

Analyzing Defect Complex Structures of PL6 in SiC: Insights from First-Principles Screening

Xin Zhao,^{1,2} Mingzhe Liu,^{1,2,*} and Chang-Kui Duan^{1,2,3,†}

¹*CAS Key Laboratory of Microscale Magnetic Resonance and School of Physical Sciences, University of Science and Technology of China, Hefei 230026, China*

²*CAS Center for Excellence in Quantum Information and Quantum Physics, University of Science and Technology of China, Hefei 230026, China*

³*Hefei National Laboratory, University of Science and Technology of China, Hefei 230088, China*

(Dated: March 19, 2025)

The PL6 color center in 4H-SiC has attracted significant research attention owing to its remarkable spin and optical properties at ambient temperatures. Unlike many color centers that require cryogenic conditions to function, the PL6 center maintains optical activity even at room temperature or higher, benefiting from the material’s high thermal conductivity and chemical stability. To elucidate the origin of PL6’s distinctive characteristics and clarify its microscopic structure in the crystal, this study conducts a comprehensive investigation of potential defect complexes through systematic first-principles calculations. Our computational approach rigorously evaluates the electronic structures and spin-related properties of various defect configurations, enabling reasonable identification of the most probable atomic arrangement responsible for the observed characteristics of PL6. Our analysis identifies a limited set of candidate structures with C_{3v} -like symmetry consistent with known experimental signatures. Among these, two defect complexes emerge as the most likely PL6 candidates. The findings suggest that targeted experimental studies, such as electron spin resonance and optically detected magnetic resonance, could further clarify the nature of the PL6 center, while additional theoretical investigations on transition matrix elements and defect formation dynamics are warranted.

I. INTRODUCTION

Spin defects in solid-state systems are promising candidate systems for quantum information science [1]. Among these candidates, divacancies in 4H-SiC have garnered significant attention due to their long coherence time [2, 3], spin-selective optical transitions [4], and telecom-wavelength fluorescence [5]. Photoluminescence (PL) centers, specifically PL1-8 [6, 7], have been reported in 4H-SiC. In particular, PL5 and PL6 exhibit similar optical and spin characteristics to those of PL1-4 [6, 8] but exhibit greater superior stability compared to PL1-4 under optical excitation [9, 10]. Experiment [8] and first-principles calculations [11] have unambiguously identified PL1-4 as the hh, kk, hk, and kh divacancies, but PL5-8 centers have not been fully identified.

Due to their highly similar properties, PL5 and PL6 are generally considered to be perturbed versions of the PL1-4 divacancy defects, influenced by their surrounding environment. One proposed explanation for the distinct properties of PL5 and PL6 related them to kh and kk divacancies located near stacking faults [12], while, challenged by subsequent experiments [13]. Divacancies generated via post-irradiation annealing (following electron or ion bombardment) [14] exist within a multifaceted point defect landscape in SiC, coexisting with intrinsic vacancies, antisite defects, and potential residual impurities inherent in the as-grown SiC material. Given

this complex defect landscape, another plausible hypothesis emerges: PL5 and PL6 are complexes formed from a divacancy paired with another intrinsic point defect. In support of this concept, a recent study combining experimental and theoretical results proposed a new atomic model for PL5. This model identifies PL5 as a kh divacancy complexed with a nearby carbon antisite (C_{Si}) defect [15]. Adopting this composite defect perspective – that PL6, like PL5, also involves a divacancy and another intrinsic defect – our current work aims to identify the possible atomic structures of PL6. We employ first-principles calculations within a constructed selection scheme to screen potential defect complex structures for PL6. This screening is based on zero-field splitting (ZFS), estimation of optical transition energy based on the Kohn-Sham (KS) gap, and binding energy of compounded defects. Ultimately, we identify two $kk + C_{Si}$ defect complex structures as the most probable candidates for PL6.

II. METHODOLOGY

A. Calculation setup

The electronic structure calculations were performed using the Vienna *ab initio* Simulation Package (VASP) [16, 17], employing the projector augmented wave (PAW) method [18] to describe the core regions of the electronic wavefunctions with recommended PAW pseudopotentials adopted. The Revised Perdew-Burke-Ernzerhof for solids functional [19] was utilized. The plane-wave cutoff en-

* duguex@ustc.edu.cn

† ckduan@ustc.edu.cn

ergy was set to 520 eV, with a $12 \times 12 \times 2$ Monkhorst-Pack k-point mesh used for the primitive cell and a single Γ point for the expanded supercell. The convergence criterion was set to 10^{-6} eV for the self-consistent field calculation and 0.01 eV/Å for the ionic relaxation. The ZFS matrix was calculated using a formalism that employs KS orbitals from periodic density functional calculations [20] with a home-built code. The PAW correction [21] and spin decontamination [22] were not considered here, and the accounted error was considered in the final results instead.

For the defect calculations, a cubic-like supercell was constructed to host the defect. When the defect was generated in the initial perfect cell, small random displacements were applied to all atomic coordinates, then the structure was relaxed until the force criterion was satisfied. This procedure was intended to exclude the influence of the initial configuration selection on the final obtained structure.

B. Determining Candidate Compounded Defects

Experimental observations show that the rhombic ZFS parameter E of PL6 is almost zero [6, 8], suggesting the principal axis of PL6 is parallel to the c -axis. Consistent with this, angle-resolved measurements also indicate a C_{3v} -like symmetry for PL6 [13]. Based on these experimental findings and our prior considerations, hh and kk are proposed as parent models for PL6. To search for the possible defect complex structure as a variant of hh or kk, a cubic-like supercell with basis vectors $5\mathbf{a}$, $3\mathbf{a}+6\mathbf{b}$, $2\mathbf{c}$ (where $(\mathbf{a}, \mathbf{b}, \mathbf{c})$ are the basis vectors of the primitive cell) was constructed. In the first stage, a hh or kk defect was generated, with its middle placed at the center of the supercell. A cylinder with a height of 8 Å and a base radius of 7 Å centered at the defect center was chosen as the total selection range for candidates. Next, the C_{3v} symmetry of hh and kk was used to exclude redundant atom sites in the cylinder structure. For the remaining sites, we only consider the neutral antisite defect, i.e., the selection is conducted on the neutral complex defect consisting of hh/kk and antisite). The final selection range contains 116 cases, 56 for hh and 60 for kk. Our selection range covers all the antisites that may have a significant impact on the divacancies properties, as the spin density distribution of the defect does not uniformly decay with distance from the hh/kk center (see Fig. ?? in the Supplemental Material [23]).

PL6 exhibits an $S = 1$ ground state with overall similar but distinct properties compared to PL1-4. This implies that the electron numbers of PL6 must be even, and its electronic configuration should resemble that of divacancy defects. Crucially, introducing an additional vacancy would lead to a state with $S \neq 1$, thereby definitively excluding vacancy-related configurations from consideration. Regarding antisite defects, since C and Si act as isovalent substituents, a neutral antisite defect com-

bined with a divacancy would alter the local structure but maintain a similar electronic environment, thus preserving the fundamental spin and optical properties. Although the ± 2 charge state also satisfies the even electron number requirement, its electronic configuration significantly deviates from the divacancy case. Consequently, this study focuses exclusively on the hh/kk-type defect complexes incorporating neutral antisite defects.

C. Screening Methodology for the PL6 Center Identification

To systematically identify the microscopic origin of the PL6 center in SiC, we established a multi-criteria screening framework that synergistically combines spin, optical, and thermodynamic properties. The selection criteria were strategically chosen to balance computational feasibility with experimental relevance, prioritizing three key aspects: (1) Consistency with experimentally measured ZFS parameters; (2) Compatibility with photoluminescence characteristics through KS level analysis; (3) Thermodynamic stability of defect complexes. This multi-property approach enables effective discrimination among thousands of possible defect configurations while maintaining manageable computational costs.

1. ZFS Parameter Calibration and Error-Tolerant Thresholds

The ZFS matrix \mathbf{D} dominates the spin Hamiltonian of a defect center. With a proper choice of axes, it can be diagonalized, yielding two parameters that characterize the energy splitting of spin states [24]:

$$D = \frac{3}{2}D_{zz}, \quad E = \frac{1}{2}(D_{yy} - D_{xx}). \quad (1)$$

Note that experimentally measured E values correspond to their absolute magnitudes. The ZFS parameters (D , E) serve as critical fingerprints for spin defects. To address systematic errors in our DFT implementation (including PAW correction and spin decontamination errors), we performed benchmark calculations on the four well-characterized divacancies (PL1-4, i.e., hh, kk, hk, kh defects), as shown in Table I. The calculated D values are 10% systematically overestimated and the calculated E values have ± 10 MHz fluctuations compared to experimental data. To ensure comprehensive coverage of potential PL6 candidates while accounting for these errors, we established conservative thresholds:

- $D \in [1.365, 1.706]$ GHz ($1.0\text{--}1.25 \times$ experimental $D = 1.365$ GHz)
- $|E| \leq 20$ MHz (experimental $E = 0$ MHz ± 20 MHz)

This error-tolerant criterion accommodates computational uncertainties and potential variations in local crystal environments.

TABLE I. Comparison of D and E between experiment and calculation, the experimental data are from Ref [8]

Divacancies	D (GHz)		E (MHz)	
	expt	calc	expt	calc
PL1(hh)	1.336	1.506	0	6.4
PL2(kk)	1.305	1.455	0	-4.3
PL3(kh)	1.222	1.395	82	-61
PL4(hk)	1.334	1.452	18.6	29

2. KS Level Difference as ZPL Predictor in Defect Screening

The photoluminescence characteristics provide critical complementary signatures for defect identification. For the C_{3v} symmetry divacancies, the ZPL originates from the spin-allowed ${}^3E \rightarrow {}^3A_2$ transition [25], corresponding to two specific occupations of KS orbitals differed by promoting an electron from the a_1 orbital to the e orbital in the minority spin channel. The calculation of ZPL of PL1-4 has been detailed and tested among supercell size, k-point mesh, and functional selection [11]. However, such calculations are computationally consumption (e.g., HSE06 functional, a Γ -only calculation with a supercell of 2400 atoms, or a calculation with $4 \times 4 \times 4$ k -mesh for a 96-atom supercell) [11, 26].

The observed 0.1 eV redshift in ZPL of PL6 over the hh/kk divacancies [8, 9] suggests a perturbation of the splitting between KS orbitals from an antisite defect. We establish a computationally efficient proxy for ZPL shifts through KS level analysis: the energy difference between the highest occupied (a_1) and lowest unoccupied (e) minority spin states systematically correlates with experimental ZPL trends in benchmarked defects (PL1-4). This relationship arises because ZPL energies and KS splitting respond proportionally to the perturbation. By requiring candidate complexes to exhibit enhanced KS splitting compared to isolated hh/kk centers, we effectively screen for structures capable of reproducing PL6's characteristic ZPL shift.

3. Binding Energy for Stability of Complex Defects

Given that PL6 likely forms through radiation-induced defect aggregation rather than thermal equilibrium processes, we employed binding energy (E_b) rather than formation energy to assess the relative stability of candidate defects. Taking hh as an example, the binding energy is defined as [27]:

$$E_b = E^f[\text{hh} + \text{antisite}] - E^f[\text{hh}] - E^f[\text{antisite}], \quad (2)$$

where E^f is the formation energy of point defects. Negative E_b values indicate exothermic complex formation, serving as a necessary (though not sufficient) condition for stability. While full thermodynamical analysis would require considering formation pathways [28] and configurational entropy [29], our screening conservatively requires $E_b < 0$ to filter physically plausible complexes.

As a summary, based on experimental measurements yielding $D = 1.365$ GHz and $E = 0$ MHz for the PL6 center, we define the selection criteria for its spin properties as follows: D within $1.365 \times [1, 1.25]$ GHz and E within $[-20, 20]$ MHz. To account for the observed ZPL blue shift of PL6 relative to hh and kk, we require PL6's KS gap to exceed those of its reference hh/kk. Additionally, a negative binding energy is imposed to ensure the stability of the defect structure. Despite the intentionally permissive criteria, the geometric and electronic constraints collectively yield only a few configurations, demonstrating remarkable latent selectivity in defect screening.

III. RESULTS AND DISCUSSION

A. The Possible PL6 Structure

After applying the screening strategy to the 116 candidates, only 12 configurations remain, as listed in Table II. To systematically characterize these surviving configurations, the unperturbed divacancy, and associated antisite defects are labeled by a grid-based positional encoding scheme. The numerical indices following an antisite symbol specify its position relative to the V_{Si} of the divacancy using grid coordinates along the \mathbf{a} -, \mathbf{b} -, and \mathbf{c} -axes, where negative displacements are denoted by overlined numbers. These coordinate axes are defined according to a gridded supercell with spacings of 1.540 Å, 0.889 Å, and 0.628 Å along each respective axis. Complete implementation details with visual examples are provided in the Supplemental Material [23].

TABLE II. Potential structures of PL6 obtained and their ZFS parameters D and E , KS gap, and binding energy E_b .

defect	D (GHz)	E (MHz)	KS gap (eV)	E_b (eV)
hh	1.506	6.4	1.117	–
kk	1.455	-4.3	1.141	–
kk + $C_{\text{Si}}(0, 0, \bar{8})$	1.478	-4.3	1.176	-0.204
kk + $C_{\text{Si}}(0, 0, 8)$	1.554	0.3	1.207	-0.083
kk + $C_{\text{Si}}(3, 3, 0)$	1.477	18.7	1.151	-0.035
kk + $C_{\text{Si}}(\bar{1}, \bar{1}, \bar{12})$	1.464	1.0	1.149	-0.024
kk + $C_{\text{Si}}(2, 0, \bar{8})$	1.469	-16.3	1.158	-0.020
hh + $C_{\text{Si}}(\bar{1}, \bar{1}, \bar{12})$	1.518	-10.0	1.127	-0.014
kk + $C_{\text{Si}}(0, \bar{2}, 12)$	1.473	9.7	1.155	-0.014
hh + $C_{\text{Si}}(2, 2, \bar{12})$	1.516	-11.0	1.129	-0.007
hh + $C_{\text{Si}}(\bar{1}, \bar{1}, 12)$	1.525	-14.7	1.129	-0.006
hh + $C_{\text{Si}}(3, 1, \bar{8})$	1.510	12.6	1.122	-0.004
kk + $C_{\text{Si}}(3, 1, 12)$	1.461	13.7	1.142	-0.004
kk + $C_{\text{Si}}(3, \bar{3}, \bar{8})$	1.459	-13.3	1.142	-0.001

A notable feature of the results is that all the binding energies are relatively weak, but for $kk + C_{Si}(0, 0, \bar{8})$, with a value of -0.204 eV, while all the others are at or lower than 10^{-2} eV. This indicates that for most candidates, the attraction between the divacancy and antisite defect is weak, leading to defect complexes with limited stability. Another feature is that most of the candidates possess an E whose absolute value is in the range of 10 to 20 MHz. A more stringent screening criterion on E (absolute value within 10 MHz) thus yields the following candidates: $kk + C_{Si}(0, 0, 8)$, $kk + C_{Si}(0, 0, \bar{8})$, $kk + C_{Si}(\bar{1}, \bar{1}, \bar{1}\bar{2})$ and $kk + C_{Si}(0, \bar{2}, 12)$. Additionally, the remaining candidates show weak KS gap enhancement relative to the original kk divacancy defect, which is consistent with the small binding energy. Among these candidates, the most enhanced KS level splitting is $kk + C_{Si}(0, 0, 8)$ and $kk + C_{Si}(0, 0, \bar{8})$. Considering all these aspects, $kk + C_{Si}(0, 0, \bar{8})$ and $kk + C_{Si}(0, 0, 8)$ are the most likely PL6 candidates.

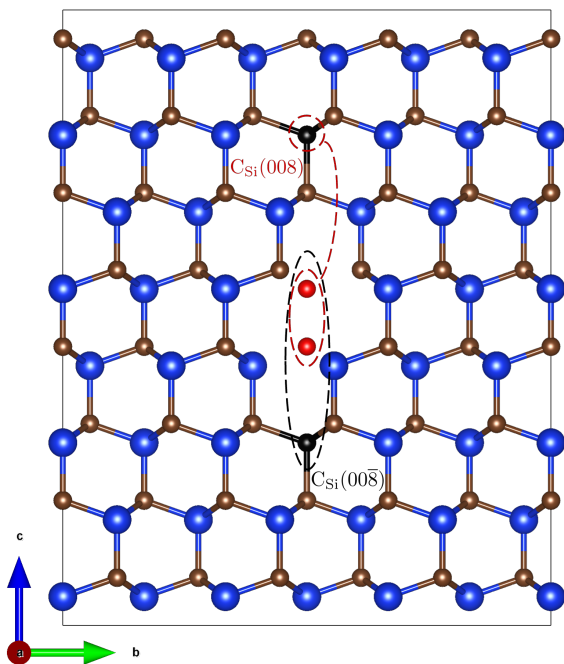


FIG. 1. The structure of the most possible PL6 candidates $kk + C_{Si}(0, 0, \bar{8})$ and $kk + C_{Si}(0, 0, 8)$. The kk divacancy is shown in red, and the C_{Si} antisite defect is shown in black.

Fig. 1 shows the detailed atomic configurations of $kk + C_{Si}(0, 0, \bar{8})$ and $kk + C_{Si}(0, 0, 8)$ defect complexes. Both structures comprise a kk divacancy and a C_{Si} antisite defect along the $[001]$ direction. These configurations exhibit C_{3v} symmetry, consistent with experimental observations indicating that PL6 is a C_{3v} -like center [13].

Apart from the difference in local environment between $kk + C_{Si}(0, 0, \bar{8})$ and $kk + C_{Si}(0, 0, 8)$, the dominant difference between them is the distance between the kk center and the antisite, which is 4.10 Å for $kk + C_{Si}(0, 0, \bar{8})$

and 6.00 Å for $kk + C_{Si}(0, 0, 8)$. The longer distance in $kk + C_{Si}(0, 0, 8)$ leads to a weaker interaction between the kk and the antisite, which is consistent with its smaller binding energy. For these two defects, we further calculated the actual ZPL energy by using constrained DFT calculation and the $0/1$ - charge transition level by the PBEsol functional. While this set of computational parameters cannot reliably reproduce experimental ZPL values, it can still capture relative shifts between different configurations. This allows for a comparative analysis of trends despite the absolute discrepancy. A comparison of the results with kk is shown in Table III. $kk + C_{Si}(0, 0, 8)$ shows a larger ZPL shift of about 0.13 eV than kk , while the ZPL shift of $kk + C_{Si}(0, 0, \bar{8})$ is only about 0.03 eV. Moreover, the $0/1$ - charge transition level of $kk + C_{Si}(0, 0, 8)$ is closer to the CBM than kk , consistent with the experimental charge dynamics model [9]. Thus, though $kk + C_{Si}(0, 0, 8)$ has a relatively small binding energy, it is the most possible PL6 candidate. Although the C_{Si} is closer to the kk center in $kk + C_{Si}(0, 0, \bar{8})$, the properties of the divacancy mainly arise from the dangling bond of the C atom, which originates from the V_{Si} inside the divacancy. Although $kk + C_{Si}(0, 0, 8)$ is farther from the kk center, it is closer to the dangling bond of the kk center, which is the reason why the impact of the antisite defect on the kk center is larger in $kk + C_{Si}(0, 0, 8)$ than in $kk + C_{Si}(0, 0, \bar{8})$.

TABLE III. The calculated ZPL and $0/1$ - charge transition level of $kk + C_{Si}(0, 0, \bar{8})$ and $kk + C_{Si}(0, 0, 8)$, with kk also listed for comparison. $E_{0/-1}^{CBM}$ represents the distance between the $0/1$ - level and the CBM.

defect	ZPL (eV)	$E_{0/-1}^{CBM}$
kk	1.024	0.951
$kk + C_{Si}(0, 0, \bar{8})$	1.055	0.962
$kk + C_{Si}(0, 0, 8)$	1.158	0.934

B. Potential Experimental Verification

In the above section, we identified the most promising PL6 candidates, $kk + C_{Si}(0, 0, \bar{8})$ and $kk + C_{Si}(0, 0, 8)$, through first-principles screening based on ZFS, ZPL, and binding energy. More experimental data are needed to verify the identification. In SiC, Si and C have stable isotopes with non-zero nuclear spins, namely ^{29}Si and ^{13}C , with nuclear gyromagnetic ratios of -8.465 MHz/T and 10.705 MHz/T, respectively. The hyperfine interaction between nuclear spin and electron spin can be observed in ESR or ODMR spectra, providing additional signatures for defect structure identification.

The 3×3 hyperfine tensor \mathbf{A}^I consists of an isotropic part (the Fermi contact term) $\mathbf{A}_{\text{iso}}^I$ and an anisotropic part $\mathbf{A}_{\text{ani}}^I$, which are expressed as:

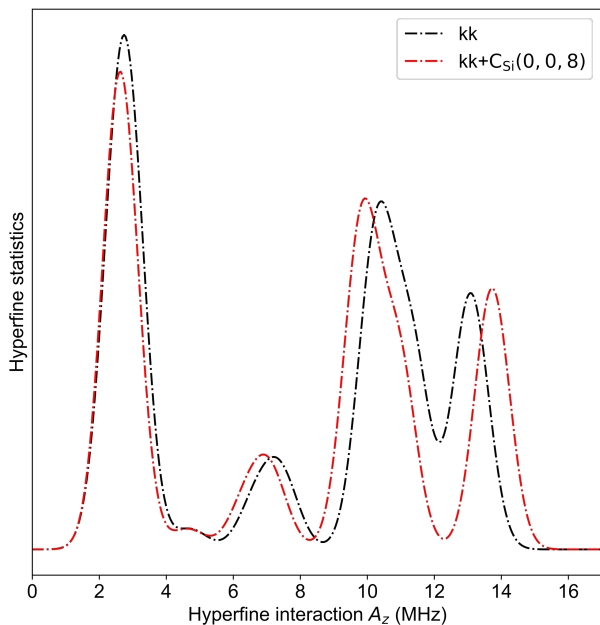


FIG. 2. The distribution of the A_z component for the kk and $kk + C_{Si}(0,0,8)$ defects. The smooth curve represents the sum of Gaussian distributions, with the mean value given by A_z and a standard deviation of 0.5 MHz. The isotopic abundances of ^{29}Si and ^{13}C are also considered.

$$(\mathbf{A}_{iso}^I)_{ij} = \frac{2}{3} \frac{\mu_0 \gamma_e \gamma_I}{\langle S_z \rangle} \delta_{ij} \int \delta_T(\mathbf{r}) \rho_s(\mathbf{r} + \mathbf{R}_I) d\mathbf{r}, \quad (3)$$

$$(\mathbf{A}_{ani}^I)_{ij} = \frac{\mu_0 \gamma_e \gamma_I}{4\pi \langle S_z \rangle} \int \frac{\rho_s(\mathbf{r} + \mathbf{R}_I)}{r^3} \frac{3r_i r_j - \delta_{ij} r^2}{r^2} d\mathbf{r}, \quad (4)$$

where γ_e and γ_I are the gyromagnetic ratios of the electron and nuclear spin, respectively, ρ_s is the spin density, δ_T is the Dirac delta function (approximated by a smeared form here), and \mathbf{R}_I is the position of the nucleus [30]. The total hyperfine tensor calculations were performed using the VASP code with the PAW method and the HSE06 functional.

A key difference between ^{13}C and ^{29}Si is the opposite sign of their gyromagnetic ratios. Consequently, replacing a Si atom site with a C atom leads to a significant change in the sign of the hyperfine tensor at that site. However, the sign of the hyperfine tensor is not directly observable in ESR or ODMR spectra. This stems from the fact that nuclear spin states always encompass both positive and negative components, resulting in redshifted and blueshifted fine-structure splitting pairs relative to the main peak. As the sign is difficult to determine experimentally, we adopt $A_z = |\vec{n}_0 \cdot \mathbf{A}^I \cdot \vec{n}_0|$, where \vec{n}_0 is along the c-axis (the principal axis of the \mathbf{D} tensor), as a characteristic parameter for hyperfine coupling. Furthermore, we analyze the statistical distribution of A_z , which is independent of any specific site within the defect complex. A more detailed discussion can be found in

the Supplement Material [23]. The results are presented in Fig. 2.

The statistical distribution of A_z for $kk + C_{Si}(0,0,\bar{8})$ is almost identical to that of kk (see Fig. ?? in Supplement Material [23]) and is omitted here for brevity. The primary difference between $kk + C_{Si}(0,0,8)$ and kk is a redshift of approximately 0.5 MHz in the [6, 12] MHz range and a blueshift of approximately 0.7 MHz in the [12, 15] MHz range in the A_z distribution. These shifts are attributed to the hyperfine interaction with ^{29}Si nuclei. As outlined in Eqs. (3) and (4), the hyperfine tensor is governed by the spin density distribution, which localizes predominantly around the V_{Si} in the positive z -direction. While the C_{Si} defect reverses the sign of the hyperfine interaction at its site (discussed earlier), it also induces a slight perturbation to the spin density at neighboring lattice sites. Since the $C_{Si}(0,0,\bar{8})$ component is positioned outside the region of significant spin density (as shown in Fig. ??), the perturbation to the spin density is weak. This results in A_z distribution is nearly identical to that of the isolated kk divacancy. In contrast, the distinct A_z behavior observed for $kk + C_{Si}(0,0,8)$ originates primarily from spatial perturbations caused by the proximal C_{Si} defect, rather than the sign reversal of the hyperfine interaction itself.

It is important to note that our analysis focuses on comparing the calculated hyperfine coupling of kk and $kk + C_{Si}(0,0,8)$, which may exhibit systematic deviations from experimental values. However, the relative shift in hyperfine coupling is experimentally observable and provides a critical means to validate our theoretical model.

C. Other Potential Spin Defects

In previous sections, we used experimental data to screen the possible PL6 candidates and obtain the most likely candidates. However, there are also many other defects considered in our calculation that serve as good spin defects but are not PL6 candidates. Table IV lists all spin defects with binding energies at or below -0.01 eV, which are potentially stable, though formation dynamics were not considered. The properties of divacancies primarily originate from the C dangling bonds formed by the V_{Si} within the divacancy. Introducing a nearest-neighbor antisite Si_C disrupts these C dangling bonds, resulting in an $S = 0$ ground state, as observed in the $kk + Si_C(\bar{1}, \bar{1}, 1)$ and $hh + Si_C(\bar{1}, \bar{1}, 1)$ configurations. Electron pairing in these defects enhances their stability relative to others. Besides, most Si_C -introduced defect complexes exhibit a significant reduction in crystal field splitting, leading to a lower-energy PL (less than 1.0 eV) or complete PL quenching, rendering them absent in PL spectra. Certain defects also display large $|E|$ (300-400 MHz), whose resonances are too widely separated in ESR or ODMR spectra for unambiguous identification. Moreover, for distant antisites, weak interactions with the central di-

TABLE IV. In addition to the previously analyzed systems, spin defects with negative binding energies are included in this comprehensive analysis. For each defect, the ZFS parameters D and E , the angle θ between the principal axis of D_{zz} and the lattice c -axis, the KS gap, and the binding energy E_b are listed. The identification of the defects is also listed. The term “red-shifted PL” is used to indicate that the ZPL of the defect is substantially red-shifted relative to those of the PL1-4. The term “undetectable” is used to label those defects with an excessively large E , which are typically not considered in the related ESR or ODMR experiments. For each defect with identification, the reason for the identification is highlighted with an underline. Some candidate spin centers without enough evidence for identification are marked with bolded “unknown”.

defect	spin	D (GHz)	E (MHz)	θ	KS gap (eV)	E_b (eV)	identification
hh	2	1.506	6.4	0.1	1.118	–	PL1
kk	2	1.455	-4.3	0.2	1.141	–	PL2
kh	2	1.395	-61	70.8	1.111	–	PL3
hk	2	1.452	29	109.9	1.137	–	PL4
kk + Si _C ($\bar{1}, \bar{1}, 1$)	0	0.000	0.0	–	0.555	-4.771	–
hh + Si _C ($\bar{1}, \bar{1}, 1$)	0	0.000	0.0	–	0.653	-4.822	–
kk + C _{Si} ($0, \bar{2}, \bar{4}$)	2	1.545	-26.9	0.0	1.137	-0.964	unknown
hh + C _{Si} ($\bar{1}, \bar{1}, \bar{4}$)	2	1.607	-126.1	1.1	1.154	-0.937	unknown
kk + Si _C ($2, 0, \bar{3}$)	2	1.411	-23.3	177.5	<u>0.951</u>	-0.810	red-shifted PL
hh + Si _C ($\bar{1}, \bar{3}, \bar{3}$)	2	1.470	-109.9	4.3	<u>0.971</u>	-0.754	red-shifted PL
kk + Si _C ($3, \bar{1}, 1$)	2	1.287	144.7	0.8	<u>0.899</u>	-0.387	red-shifted PL
hh + Si _C ($3, \bar{1}, 1$)	2	1.338	158.9	1.6	<u>0.880</u>	-0.363	red-shifted PL
kk + Si _C ($0, 0, 5$)	2	0.981	-6.9	0.2	<u>0.603</u>	-0.339	red-shifted PL
kk + C _{Si} ($2, 2, 0$)	2	1.306	<u>417.5</u>	5.9	1.021	-0.338	undetectable
hh + Si _C ($\bar{2}, \bar{2}, 5$)	2	1.049	94.5	1.6	<u>0.798</u>	-0.328	red-shifted PL
kk + C _{Si} ($\bar{1}, \bar{1}, 4$)	2	1.702	<u>-384.4</u>	7.6	1.038	-0.327	undetectable
hh + C _{Si} ($\bar{1}, \bar{3}, 0$)	2	1.347	<u>459.9</u>	7.0	1.001	-0.321	undetectable
hh + Si _C ($\bar{1}, \bar{1}, \bar{7}$)	2	1.425	<u>-439.8</u>	11.2	<u>0.664</u>	-0.315	undetectable
hh + C _{Si} ($\bar{1}, \bar{1}, 4$)	2	1.769	<u>-433.2</u>	8.5	1.034	-0.309	undetectable
kk + Si _C ($4, 0, \bar{3}$)	2	1.487	29.7	0.8	1.040	-0.253	unknown
kk + Si _C ($0, \bar{2}, \bar{7}$)	2	1.403	95.6	1.7	<u>0.900</u>	-0.241	red-shifted PL
hh + Si _C ($4, 0, \bar{3}$)	2	1.544	-27.4	1.0	1.041	-0.238	unknown
kk + C _{Si} ($0, 0, \bar{8}$)	2	<u>1.478</u>	<u>-4.3</u>	<u>0.3</u>	<u>1.176</u>	<u>-0.204</u>	PL6
hh + C _{Si} ($2, 2, \bar{4}$)	2	1.523	-36.7	0.6	1.138	-0.183	unknown
kk + C _{Si} ($\bar{2}, \bar{2}, \bar{4}$)	2	<u>1.460</u>	<u>-43.8</u>	0.2	<u>1.153</u>	-0.159	hk-like
hh + C _{Si} ($0, \bar{2}, \bar{8}$)	2	<u>1.527</u>	<u>-14.8</u>	<u>179.5</u>	<u>1.111</u>	-0.098	hh mixed
kk + C _{Si} ($4, 0, 0$)	2	1.319	-39.1	0.6	1.031	-0.092	unknown
kk + C _{Si} ($0, 0, 8$)	2	<u>1.554</u>	<u>0.3</u>	<u>0.3</u>	<u>1.207</u>	-0.083	PL6
hh + C _{Si} ($4, 0, 0$)	2	1.387	-32.1	0.7	1.038	-0.082	unknown
kk + Si _C ($2, 0, 5$)	2	1.258	60.3	1.4	<u>0.839</u>	-0.066	red-shifted PL
hh + C _{Si} ($\bar{2}, \bar{2}, \bar{8}$)	2	1.491	-35.4	1.5	1.098	-0.058	unknown
hh + Si _C ($\bar{2}, \bar{2}, \bar{11}$)	2	1.486	-44.5	0.6	<u>1.001</u>	-0.047	red-shifted PL
hh + Si _C ($4, \bar{2}, 5$)	2	1.484	-23.3	0.2	<u>0.903</u>	-0.041	red-shifted PL
kk + C _{Si} ($2, 0, 8$)	2	<u>1.453</u>	<u>46.1</u>	1.3	<u>1.124</u>	-0.037	hk-like
kk + C _{Si} ($3, 3, 0$)	2	<u>1.477</u>	<u>18.7</u>	0.6	<u>1.151</u>	-0.035	hk-like
kk + Si _C ($4, 0, 5$)	2	1.458	-36.8	0.1	<u>0.900</u>	-0.029	red-shifted PL
kk + C _{Si} ($\bar{1}, \bar{1}, \bar{12}$)	2	<u>1.464</u>	<u>1.0</u>	<u>179.8</u>	<u>1.149</u>	-0.024	kk mixed
kk + Si _C ($3, \bar{3}, 5$)	2	1.466	-21.7	0.4	<u>0.885</u>	-0.024	red-shifted PL
kk + C _{Si} ($2, 0, \bar{8}$)	2	<u>1.469</u>	-16.3	<u>0.3</u>	<u>1.158</u>	-0.020	kk mixed
kk + C _{Si} ($0, \bar{2}, 12$)	2	<u>1.473</u>	<u>9.7</u>	<u>0.1</u>	<u>1.155</u>	-0.014	kk mixed
hh + C _{Si} ($\bar{1}, \bar{1}, \bar{12}$)	2	<u>1.518</u>	<u>-10.0</u>	<u>0.1</u>	<u>1.127</u>	-0.014	hh mixed
hh + Si _C ($3, \bar{1}, \bar{7}$)	2	<u>1.506</u>	<u>-9.6</u>	<u>0.6</u>	1.072	-0.013	hh mixed
hh + C _{Si} ($0, \bar{2}, \bar{8}$)	2	<u>1.559</u>	<u>-13.2</u>	<u>0.6</u>	<u>1.109</u>	-0.010	hh mixed

vacancy result in small perturbation, making them hard to distinguish from their parent divacancies. Notably, many defects labeled as “kh-like” exhibit spin properties similar to the hk divacancy while retaining ZPL energies near their original values. However, the principal axis of the D_{zz} remains approximately aligned with the c -axis,

a feature resolvable through angle-resolved EPR experiments.

Among numerous stable defect complexes identified, only a limited subset demonstrates characteristics worthy of investigation as potential spin centers with distinct properties. Apart from the plausible PL6 candi-

dates, $kk + C_{Si}(0, 0, \bar{8})$ and $kk + C_{Si}(0, 0, 8)$, eight additional stable defect complexes, highlighted in bold within Table IV, emerge as effective spin centers. Notably, the $hh + Si_C(4, 0, \bar{3})$ and $kk + Si_C(4, 0, \bar{3})$ exhibit similar structural compositions and comparable properties. Although their KS level gaps are narrower than those of PL1-4, resulting in lower ZPL energies, their D and E parameters remain comparable to those of PL1-4. A distinct pair, $kk + C_{Si}(4, 0, 0)$ and $hh + C_{Si}(4, 0, 0)$, demonstrates reduced ZPL energies alongside significantly smaller D values. The most stable spin defect complexes, $kk + C_{Si}(0, \bar{2}, \bar{4})$ and $hh + C_{Si}(\bar{1}, \bar{1}, \bar{4})$, exhibit ZPL energies within the PL1-4 spectral range. While $kk + C_{Si}(0, \bar{2}, \bar{4})$ shares similarities with the hk defect, it features an enhanced D parameter. The $hh + C_{Si}(\bar{1}, \bar{1}, \bar{4})$ complex displays an exceptionally large E value and a D parameter exceeding those of PL1-4 while simultaneously demonstrating superior thermodynamic stability based on binding energy analysis. Additional notable configurations include $hh + C_{Si}(2, 2, \bar{4})$ (with elevated ZPL energy, increased $|E|$ magnitude, and higher D value relative to the hh defect), and $hh + C_{Si}(\bar{2}, \bar{2}, 8)$ (reduced ZPL energy while maintaining hk -like defect characteristics).

We have not considered exploring the transition profiles [31–33] of the PL6 candidates and other spin defects, which could serve as additional criteria. The dynamics of the formation of the defect complex could also be explored to further judge the stability of the defect complex and guide the synthesis of the defect complex in experiments.

IV. CONCLUSION

In conclusion, we have identified the most possible PL6 candidates, $kk + C_{Si}(0, 0, \bar{8})$ and $kk + C_{Si}(0, 0, 8)$, by the first-principles screening on ZFS, ZPL, and binding energy. The C_{Si} antisite defect is the most probable antisite defect in the SiC crystal, and the C_{3v} symmetry of the defect complex is consistent with the experimental hypothesis. The experimental verification of the candidates could be conducted by the ESR or ODMR spectra, focusing on the hyperfine interaction between the nuclear spin and the electron spin. We also found eight other stable defect complexes that could serve as effective spin centers. Future work could include exploring the dynamics of the formation of the defect complex and further experimental verification of the candidates.

ACKNOWLEDGMENTS

The numerical calculations in this paper have been done on the supercomputing system in the Supercomputing Center of University of Science and Technology of China. The *vaspkit* code [34] was used to generate calculation files and analyze the results. *Vesta* [35] was used to visualize the structure.

-
- [1] G. Wolfowicz, F. J. Heremans, C. P. Anderson, S. Kanai, H. Seo, A. Gali, G. Galli, and D. D. Awschalom, *Nat. Rev. Mater.* **6**, 906 (2021).
- [2] D. J. Christle, A. L. Falk, P. Andrich, P. V. Klimov, J. U. Hassan, N. T. Son, E. Janzén, T. Ohshima, and D. D. Awschalom, *Nat. Mater.* **14**, 160 (2015).
- [3] C. P. Anderson, E. O. Glen, C. Zeledon, A. Bourassa, Y. Jin, Y. Zhu, C. Vorwerk, A. L. Crook, H. Abe, J. Ul-Hassan, T. Ohshima, N. T. Son, G. Galli, and D. D. Awschalom, *Sci. Adv.* **8**, eabm5912 (2022).
- [4] D. J. Christle, P. V. Klimov, C. F. de las Casas, K. Szász, V. Ivády, V. Jokubavicius, J. U. Hassan, M. Syväjärvi, W. F. Koehl, T. Ohshima, N. T. Son, E. Janzén, A. Gali, and D. D. Awschalom, *Phys. Rev. X* **7**, 021046 (2017).
- [5] Z. Mu, A. Rasmita, J. Yang, X. Li, and W. Gao, *Adv. Quantum Technol.* **4**, 2100076 (2021).
- [6] A. L. Falk, B. B. Buckley, G. Calusine, W. F. Koehl, V. V. Dobrovitski, A. Politi, C. A. Zorman, P. X. L. Feng, and D. D. Awschalom, *Nat. Commun.* **4**, 1819 (2013).
- [7] F.-F. Yan, A.-L. Yi, J.-F. Wang, Q. Li, P. Yu, J.-X. Zhang, A. Gali, Y. Wang, J.-S. Xu, X. Ou, C.-F. Li, and G.-C. Guo, *npj Quantum Inf.* **6**, 38 (2020).
- [8] W. F. Koehl, B. B. Buckley, F. J. Heremans, G. Calusine, and D. D. Awschalom, *Nature* **479**, 84 (2011).
- [9] G. Wolfowicz, C. P. Anderson, A. L. Yeats, S. J. Whiteley, J. Niklas, O. G. Poluektov, F. J. Heremans, and D. D. Awschalom, *Nat. Commun.* **8**, 1876 (2017).
- [10] Z.-X. He, J.-Y. Zhou, Q. Li, W.-X. Lin, R.-J. Liang, J.-F. Wang, X.-L. Wen, Z.-H. Hao, W. Liu, S. Ren, H. Li, L.-X. You, R.-J. Zhang, F. Zhang, J.-S. Tang, J.-S. Xu, C.-F. Li, and G.-C. Guo, *Nat. Commun.* **15**, 10146 (2024).
- [11] J. Davidsson, V. Ivády, R. Armiento, N. T. Son, A. Gali, and I. A. Abrikosov, *New J. Phys.* **20**, 023035 (2018).
- [12] V. Ivády, J. Davidsson, N. Deegan, A. L. Falk, P. V. Klimov, S. J. Whiteley, S. O. Hruszkewycz, M. V. Holt, F. J. Heremans, N. T. Son, D. D. Awschalom, I. A. Abrikosov, and A. Gali, *Nat. Commun.* **10**, 5607 (2019).
- [13] N. T. Son, D. Shafizadeh, T. Ohshima, and I. G. Ivanov, *J. Appl. Phys.* **132**, 025703 (2022).
- [14] Q.-Y. Luo, Q. Li, J.-F. Wang, P.-J. Guo, W.-X. Lin, S. Zhao, Q.-C. Hu, Z.-Q. Zhu, J.-S. Xu, C.-F. Li, and G.-C. Guo, *Front. Phys.* **11**, 10.3389/fphy.2023.1270602 (2023).
- [15] Y. Chen, Q. Zhang, M. Liu, J. Liu, J. Zhou, P. Yu, S. Lin, Y. Teng, W. Yu, Y. Wang, C. Duan, F. Shi, and J. Du, (2025), under review.
- [16] G. Kresse and J. Hafner, *Phys. Rev. B* **47**, 558 (1993).
- [17] G. Kresse and J. Hafner, *Phys. Rev. B* **49**, 14251 (1994).
- [18] P. E. Blöchl, *Phys. Rev. B* **50**, 17953 (1994).
- [19] J. P. Perdew, A. Ruzsinszky, G. I. Csonka, O. A. Vydrov, G. E. Scuseria, L. A. Constantin, X. Zhou, and K. Burke, *Phys. Rev. Lett.* **100**, 136406 (2008).

- [20] M. J. Rayson and P. R. Briddon, *Phys. Rev. B* **77**, 035119 (2008).
- [21] Z. Bodrog and A. Gali, *J. Phys.: Condens. Matter* **26**, 015305 (2013).
- [22] T. Biktagirov, W. G. Schmidt, and U. Gerstmann, *Phys. Rev. Res.* **2**, 022024 (2020).
- [23] See Supplement Material for further information about Possible Corresponding Defect Complex Structure of PL6 in SiC.
- [24] V. Ivády, T. Simon, J. R. Maze, I. A. Abrikosov, and A. Gali, *Phys. Rev. B* **90**, 235205 (2014).
- [25] A. Gali, A. Gällström, N. T. Son, and E. Janzén, in *Mater. Sci. Forum*, Vol. 645 (2010) p. 395.
- [26] A. V. Krukau, O. A. Vydrov, A. F. Izmaylov, and G. E. Scuseria, *J. Chem. Phys.* **125**, 224106 (2006).
- [27] C. Freysoldt, B. Grabowski, T. Hickel, J. Neugebauer, G. Kresse, A. Janotti, and C. G. V. de Walle, *Rev. Mod. Phys.* **86**, 253 (2014).
- [28] E. M. Y. Lee, A. Yu, J. J. de Pablo, and G. Galli, *Nat. Commun.* **12**, 6325 (2021).
- [29] C. G. V. de Walle and J. Neugebauer, *J. Appl. Phys.* **95**, 3851 (2004).
- [30] P. E. Blöchl, *Phys. Rev. B* **62**, 6158 (2000).
- [31] Y. Jin, M. Govoni, G. Wolfowicz, S. E. Sullivan, F. J. Heremans, D. D. Awschalom, and G. Galli, *Phys. Rev. Mater.* **5**, 084603 (2021).
- [32] L. Razinkovas, M. Maciaszek, F. Reinhard, M. W. Doherty, and A. Alkauskas, *Phys. Rev. B* **104**, 235301 (2021).
- [33] Q. Quan and C.-K. Duan, *Phys. Rev. B* **111**, 075156 (2025).
- [34] V. Wang, N. Xu, J.-C. Liu, G. Tang, and W.-T. Geng, *Comput. Phys. Commun.* **267**, 108033 (2021).
- [35] K. Momma and F. Izumi, *J. Appl. Crystallogr.* **41**, 653 (2008).

Supplemental Material for Analyzing Defect Complex Structures of PL6 in SiC: Insights from First-Principles Screening

Xin Zhao and Mingzhe Liu*

*CAS Key Laboratory of Microscale Magnetic Resonance and School of Physical Sciences,
University of Science and Technology of China, Hefei 230026, China and
CAS Center for Excellence in Quantum Information and Quantum Physics,
University of Science and Technology of China, Hefei 230026, China*

Chang-Kui Duan†

*CAS Key Laboratory of Microscale Magnetic Resonance and School of Physical Sciences,
University of Science and Technology of China, Hefei 230026, China
CAS Center for Excellence in Quantum Information and Quantum Physics,
University of Science and Technology of China, Hefei 230026, China and
Hefei National Laboratory, University of Science
and Technology of China, Hefei 230088, China*

(Dated: March 19, 2025)

* duguex@ustc.edu.cn

† ckduan@ustc.edu.cn

S1. SPIN DENSITY DISTRIBUTION OF KK STRUCTURE

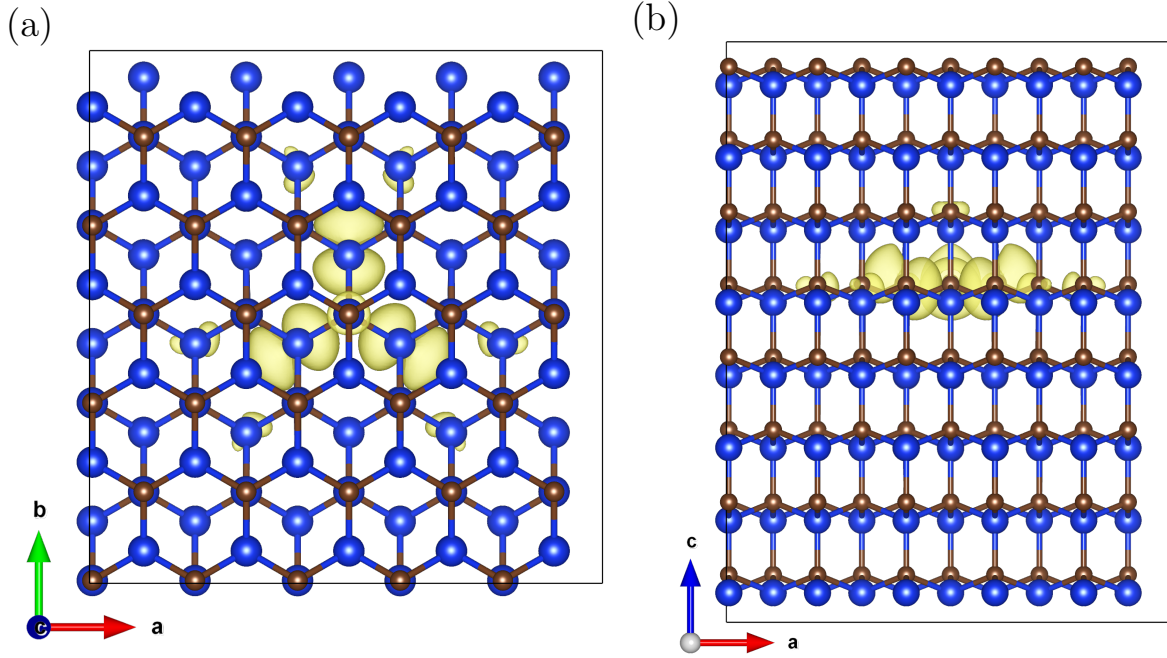


FIG. S1: Spin density distribution of the kk structure. (a) Top view; (b) Side view.

Fig. S1 shows the spin density distribution of the kk structure. The overall distribution respects the C_{3v} symmetry of the kk center. The spin density is mainly distributed around the V_{Si} center, which generates dangling C bonds. However, the spin density does not decay uniformly with distance from the V_{Si} center. The distribution is quite extended and directional within the ab plane. The zero-field splitting (ZFS) parameters and hyperfine interaction rely heavily on the spin density distribution. Therefore, when considering possible sites altering the kk center to form the PL6 center, one should not only consider the nearest neighbor sites but also other sites that are far from the center, as they may also possess relatively high spin density and should be taken into account. For the sake of generality, we consider a relatively large selection range for the possible sites of the PL6 center, which is shown in the main text.

S2. DEFECT COMPLEX NOMENCLATURE

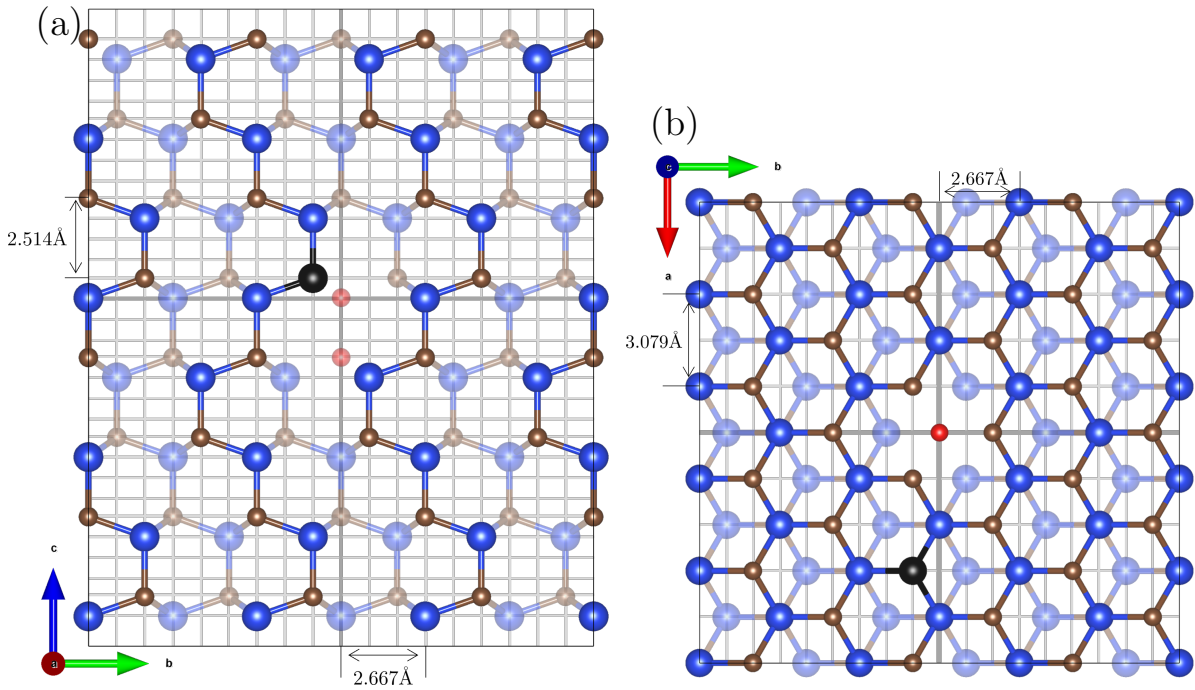


FIG. S2: Illustration of the grid division and nomenclature, using $kk + \text{Si}_C(3, \bar{1}, 1)$ as an example. The red atom indicates the vacancy position, while the dark atom represents the C_{Si} antisite. The V_{Si} location (coordinate origin) is marked with thicker, darker-colored grid lines. Arrows in (a) and (b) denote the positive directions of the \mathbf{a} -, \mathbf{b} -, and \mathbf{c} -axes. Actual grid distances are provided in the figure. (a) Side view showing grids spanning vectors \mathbf{b} and \mathbf{c} . (b) Top view showing grids spanning vectors \mathbf{a} and \mathbf{b} .

To describe defect complex structures combining a divacancy prototype and an antisite defect, we propose a naming convention: *divacancy + antisite(relative coordinates)*. Here, the *divacancy* refers to a predefined divacancy configuration, and the relative coordinates indicate the antisite defect's position relative to the V_{Si} in the divacancy. The supercell is partitioned into uniform grids along lattice vectors \mathbf{a} , \mathbf{b} , and \mathbf{c} , with spacings of 1.540 Å, 0.889 Å, and 0.628 Å, respectively. This ensures that all atomic sites correspond to grid points, and relative coordinates can be expressed as integer grid indices along these vectors, with the site of V_{Si} serving as the origin (0, 0, 0). Negative coordinates are denoted by overbars (e.g., -1 becomes $\bar{1}$). For example, in $kk + \text{Si}_C(3, \bar{1}, 1)$, the Si_C antisite is located 3 grid units along \mathbf{a} , -1 unit along \mathbf{b} , and 1 unit along \mathbf{c} relative to the V_{Si} origin, as

illustrated in Fig. S2.

S3. HYPERFINE STATISTICS OF THE POSSIBLE PL6 CENTER

The hyperfine interaction of electronic spin and nuclear spin is given by:

$$H_I = \mathbf{S} \mathbf{A} \mathbf{I} \quad (\text{S1})$$

in which \mathbf{S} and \mathbf{I} are the electronic spin and nuclear spin operators, respectively, and \mathbf{A} is the hyperfine tensor. In the experiment, by applying an external magnetic field, the directions of S_z and I_z are determined, and the hyperfine interaction can be simplified to:

$$H_I^z = S_z A_{zz} I_z \quad (\text{S2})$$

Then the fine structure splitting of the electronic spin state is $\langle S_z \rangle A_{zz} I_z$. The nuclear spin I_z is independent of the electronic spin S_z , and is directly quantized as $m_z = -I, \dots, I$. The final energy level splitting lines are always even, as there always exist $\pm \langle S_z \rangle A_{zz} m_z$. Thus, a sign change of \mathbf{A} would not be reflected in the fine structure of energy levels.

The introduction of C_{Si} centers has two effects: (i) Reversing the sign of the hyperfine interaction at the C_{Si} site, which originates from the opposite signs of the gyromagnetic ratios of Si and C. (ii) Introducing a minor perturbation to the spin density on nearby sites. The first effect, as aforementioned, is not directly measurable by the fine structure of the energy levels in an experiment. Although the second effect is measurable in principle, the subtle variations arising from C_{Si} site occupations render these distinctions experimentally challenging to resolve. Thus, to bridge theory and experiment, we analyze the statistical distribution of hyperfine values $|\vec{n}_0 \cdot \mathbf{A} \cdot \vec{n}_0|$ across all lattice sites, where \vec{n}_0 is the unit vector pointing along the c axis. These results are shown in Fig. S3, with panel (a) reproduced from the main text. The small difference between $\text{kk} + \text{C}_{\text{Si}}(0, 0, \bar{8})$ and kk aligns with the low spin density around the $\text{C}_{\text{Si}}(0, 0, \bar{8})$ site.

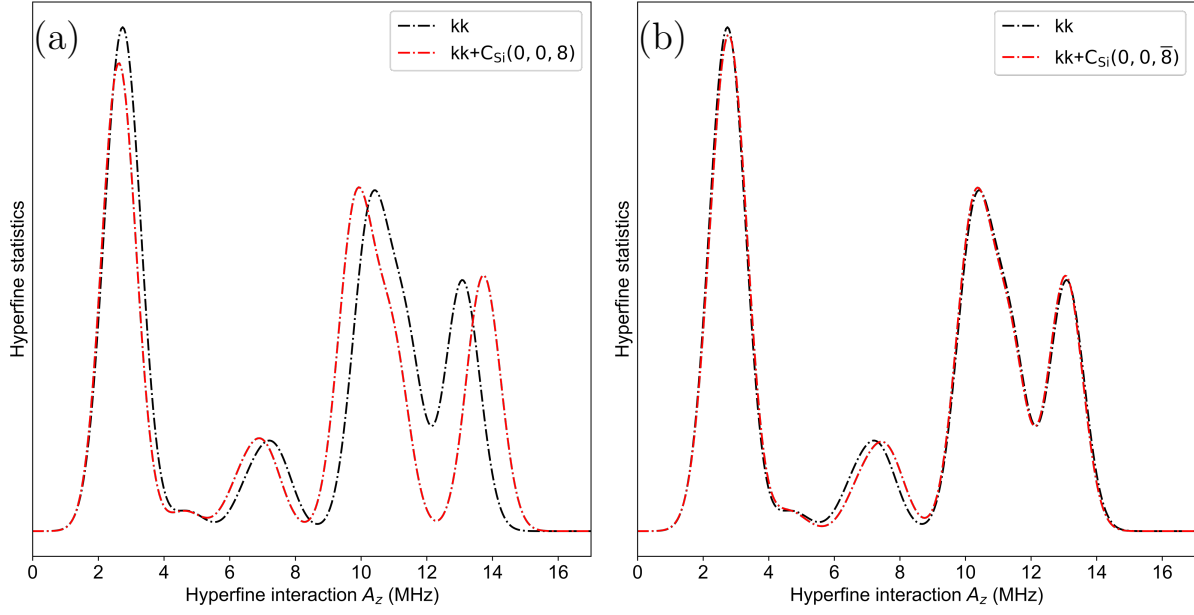


FIG. S3: Hyperfine statistics of the most probable PL6 candidates compared to the prototype kk divacancy. (a) The $kk + C_{Si}(0, 0, 8)$ configuration; (b) The $kk + C_{Si}(0, 0, \bar{8})$ configuration.